Variable Virtual Impedance-based Overcurrent Protection For Grid-forming Inverters: Small-Signal, Large-Signal Analysis and Improvement

Qoria Taoufik, Heng Wu, *Member, IEEE*, Xiongfei Wang, *Senior Member, IEEE*, Ilknur Colak, *Senior Member, IEEE*

***Abstract*—Grid-forming inverters are sensitive to large grid disturbances that may engender overcurrent due to their voltage source behavior. To overcome this critical issue and ensure the safety of the system, current limitation techniques have to be implemented. In this context, the variable virtual impedance (VI) appears as a suitable solution for this problem. The design of the variable virtual impedance basically rests on static considerations, while, its impact on the system stability and dynamics considering both small-signal and large-signal aspects can be significant. This paper proposes small-signal and nonlinear power models to assess the impact of the virtual impedance parameters on the grid current dynamics and on the angle stability. Thanks to the developed theoretical approaches in this paper, the virtual impedance ratio X/R, which is the unique degree of freedom has shown a contradictory effect on the small and large signal stability. To overcome this constraint, a Variable Transient Virtual Resistance (VRTVR) has been proposed as an additional degree of freedom to the variable virtual impedance. It acts as a transient damper to ensure the maximum angle stability margin allowed by the variable virtual impedance. The effectiveness of the proposed control has been proven through time-domain simulations.**

***Index Terms*—Grid-forming, Virtual Impedance, Current Limitation, Small-Signal Stability, Large-Signal Stability**

I. Introduction

THE rapid development of intermittent renewable generation and High Voltage Direct Current (HVDC) links yields an important increase of the penetration rate of power electronic inverters in the power transmission systems. Nowadays, power inverters have the main function of injecting the power into the main grid, while relying on synchronous machines that ensure all system needs. This operation mode is known as "Grid-following" and has several limitations e.g., their inability to operate in a standalone mode, their stability issues under weak grids and faulty conditions and their negative side effect on the system inertia [1]. These limitations call into question the reliability and security of the future electrical system dominated by power electronic inverters. To tackle these challenges, the way the inverters are controlled today should be changed from following the grid voltage to forming the grid voltage. In this perspective, the grid-forming capability appears as a promising solution since it allows the inverter to operate as a voltage source, and to mimic some characteristics of synchronous generators (i.e., emulation of the swing equation) [2]–[4].

Due to the voltage source behavior of the grid-forming inverters, the overcurrent protection requires specific attention [5]. Compared to synchronous generators (SGs) that have a high short-circuit current capability, power inverters can only cope with a few percents of overloading and two times their rated current in one millisecond [6]. Therefore, the grid-forming inverters have to be protected against extreme faults such as short-circuits, heavy load connection, line-tripping/re-closing and voltage phase jump only based on the control, while being able to remain synchronized and connected to the power system [7].

Two fundamental techniques are used to limit the current during large transients for grid-forming inverters. The first technique consists in saturating the current reference (CSA) [8]. This technique itself is implemented in different manners e.g., with and without $d-q$ axis priority [8], [9], circular technique in $\alpha-\beta$ [10] and the elliptic technique mainly used in unbalance grid conditions [11]. In practice, this technique is implemented on the inverters with cascaded inner voltage and current control loops, in which the generated current reference is saturated during overcurrent. The second current limiting strategy is based on a variable virtual impedance (VI), which emulates the effect of an impedance when the current exceeds its nominal value [12]–[15]. This method takes the advantages of dealing with overcurrent issues while keeping the voltage source behavior behind impedance of the power inverter, additionally, it can be adopted for various control structures (i.e., cascaded controls and direct controls [16], [17]). In this paper, Modular Multilevel Inverter (MMC) topology is used, and referring to [18], the MMC could be naturally driven as a controllable AC voltage source in open-loop (i.e., current control-Less), in this case, the VI is the suitable solution for overcurrent protection purpose.

The design of the VI basically rests on static considerations and do not take into account the dynamic aspects of the system [12]. To improve the dynamic response of the system including the VI, authors in [12] and [15] propose an additional virtual impedance and low-pass filters on the VI components, respectively. These solutions where limited due to their impact on the system dynamics under normal and faulty conditions. In a recent work [17], the authors investigate the impact of the VI low-pass filters (LPF) on system stability and propose

Taoufik Qoria is with Maschinenfabrik Reinhausen, Medium Voltage Power Electronics R&D Department, Germany, e-mail: (t.qoria@reinhausen.com).

Heng Wu and Xiongfei Wang are with Aalborg Universitet Teknisk-Naturvidenskabelige Fakultet, Department of Energy Technology.

Ilknur Colak is with Schneider Electric France

an optimal tuning of their cut-off frequencies to ensure a stable operation. Nevertheless, the transient response of the current is still higher than the defined threshold. This could be explained by the fact that the filters induce a delay on the VI action. In [13] and [14], the grid-forming VSC performances including only the VI have been assessed in different faulty conditions i.e., three-phase fault and grid voltage phase jump, respectively. The outcomes from these studies confirm the effectiveness of the VI to limit the current in steady state, however, the VI presents some transient oscillations exceeding the maximum current during dozens of milliseconds. The conclusions drawn from these prior works [12]–[15], [17] focus on the impact of different controls associated with the VI on the system, however, to the best of our knowledge, no works take into account the impact of the VI parameters on the system stability and dynamics. Moreover, apart from the current dynamics and the small-signal stability aspects, the transient stability including the VI is another challenge. Referring to the state of the art, the transient stability has been analysed in [19], [20], and different methods to enhance the Critical Clearing Angle (CCA) and the Critical Clearing Time (CCT) in case of a bolted fault have been proposed, i.e., the authors in [1] and [19] suggest to decrease the power reference or increase the power damping with respect to the AC voltage magnitude. Alternative solutions such as increasing the inertia constant with respect to the AC voltage magnitude [21] and boosting the reactive power injection [24] have also been suggested. Similar approaches are well summarized in [22]. Common remark about these prior works is that the VI design has not been considered as a factor that may have a significant effect on the transient stability and an impact on the effectiveness of their proposed solutions.

Based on the summarized state-of-the art, this paper proposes the following contributions:

- A simplified small-signal model of the grid-forming VSC-MMC, which is used to assess the system stability and dynamics with respect to the VI parameters.
- Large-signal stability analysis of the grid-forming VSC-MMC considering the impact of the VI parameters.
- An improved VI to enhance the transient response of the current during faults while guaranteeing the maximum transient stability margin allowed by the VI.

The effectiveness of the proposed analysis and solution are demonstrated through time-domain simulations performed in MATLAB/SimPowerSystem.

The reminder of this paper is organized as follows. In section II, the grid-forming VSC-MMC power and control structures are presented and explained. In section III, the small-signal and large signal analysis are performed to assess the impact of the VI parameters on the system. In section IV, an improved virtual impedance to enhance system dynamics is proposed. Finally, section V concludes the paper.

II. Grid-Forming-Based Modular Multilevel Inverter

The circuit diagram and the control structure of the grid-forming VSC are presented in Fig. 1 and Fig. 2, respectively.

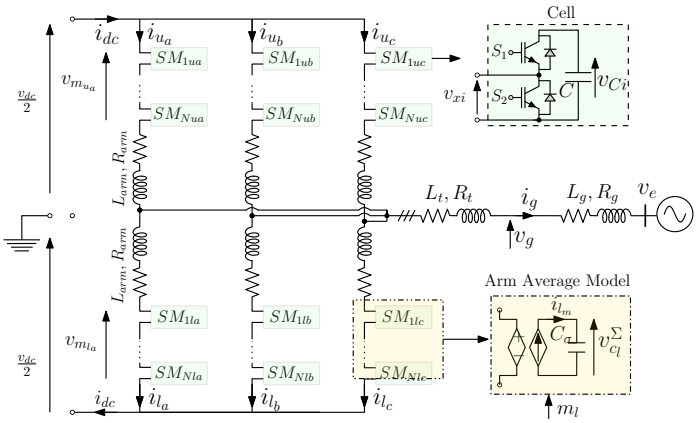

Fig. 1. Double Star Modular Multilevel Inverter topology

The VSC-MMC is supplied by a stiff DC bus u_{dc} and connected to the AC grid through an an equivalent transformer impedance L_t, R_t. The grid side is modelled by equivalent Thevenin voltage v_e in series with equivalent R_g,L_g. In contrary to a conventional 2-Level VSC often connected to the AC side through an LCL filter, the MMC does not require such a filter thanks to its ability to generate a quasi-sinusoidal voltage waveform at the output.

With regard to the control side, the outer active power control generates the voltage angle θ_m with respect to the predefined setpoints and measured power imbalance, while, the voltage magnitude $v^*_{v_{dq}}$ is directly driven to the modulation stage through the VI, where it is combined with internal voltage of the MMC v^*_z to generate the modulated voltages. Each control function illustrated in Fig. 2 is further explained in the following sections.

A. Inverter Topology and Modeling

The basic topology of a three-phase MMC is displayed in Fig. 1. Each MMC arm consists of a series connection of N cells with capacitors C. The arms are connected to a filter impedance L_{arm}, R_{arm} to form the connection between one of the DC-terminals and the AC-side. Two identical arms are connected to the upper and lower DC-terminals, respectively, to form one leg for each phase $j \in a, b, c$.

By applying the Kirchhoff's Voltage Law (KVL), the following equations can be obtained for each phase of the MMC:

$$\begin{aligned}\frac{v_{dc}}{2} = v_{mu_j} + L_{arm}\frac{d}{dt}i_{u_j} + R_{arm}i_{u_j} + (R_t + R_g)\, i_{g_j} \\ + (L_t + L_g)\frac{d}{dt}i_{g_j} + v_{e_j}\end{aligned} \tag{1}$$

$$\begin{aligned}\frac{v_{dc}}{2} = v_{ml_j} + L_{arm}\frac{d}{dt}i_{l_j} + R_{arm}i_{l_j} + (R_t + R_g)\, i_{g_j} \\ + (L_t + L_g)\frac{d}{dt}i_{g_j} + v_{e_j}\end{aligned} \tag{2}$$

In order to decouple the AC side from the DC side, (1) can be added to (2) to determine the DC side model, and (1) can be substituted from (2) to obtain the AC side model, respectively:

$$\frac{v_{dc_j}}{2} - v_{z_j} = L_{arm}\frac{d}{dt}i^{\Sigma}_{z_j} + R_{arm}i^{\Sigma}_{z_j} \tag{3}$$

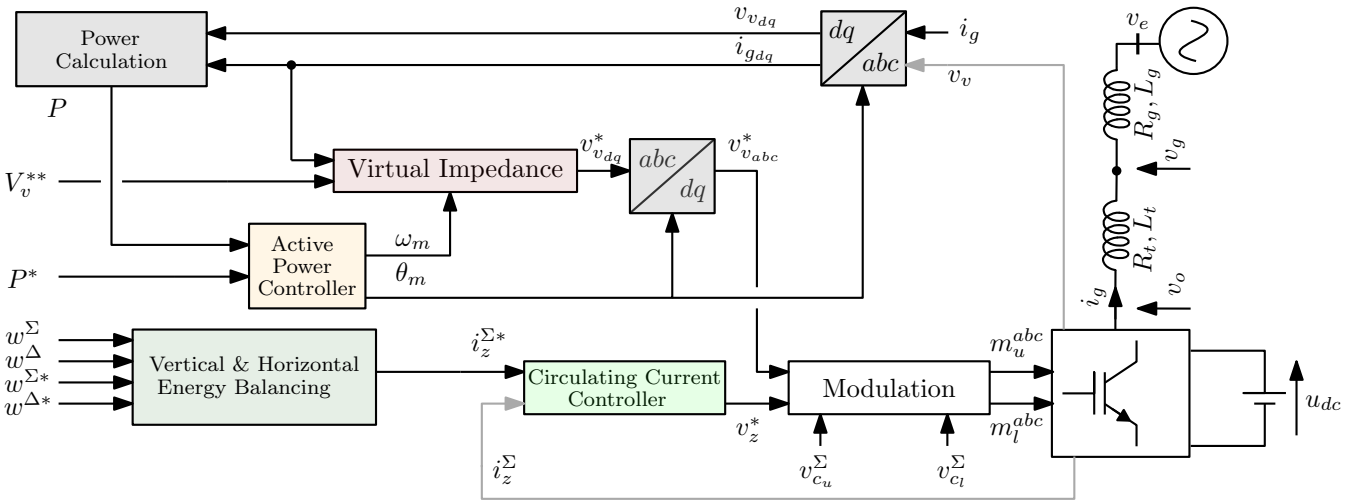

Fig. 2. General configuration of the MMC grid-forming VSC

$$v_{v_j} - v_{e_j} = (L_{eq} + L_g)\frac{d}{dt} i_{g_j} + (L_{eq} + L_g)\, i_{g_j} \tag{4}$$

with:

$$L_{eq} = \frac{L_{arm}}{2} + L_t, \quad R_{eq} = \frac{R_{arm}}{2} + R_t \tag{5}$$

$$v_{z_j} = \frac{v_{mu_j} + v_{ml_j}}{2}, \quad v_{v_j} = \frac{v_{ml_j} - v_{mu_j}}{2} \tag{6}$$

$$i_{z_j}^\Sigma = \frac{i_{u_j} + i_{l_j}}{2} \tag{7}$$

In (6) and (7), i_z^Σ, v_{z_j} and v_{v_j} denote the circulating current, the sum and difference between the upper and lower modulated voltages, respectively.

(4) can be written in the synchronous rotating frame (SRF) in per-unit as:

$$\frac{s i_{g_d}}{\omega_b} = \frac{v_{v_d} - v_{e_d}}{L_{eq} + L_g} - \left(\frac{R_{eq} + R_g}{L_{eq} + L_g}\right) i_{g_d} + \omega_g i_{g_q} \tag{8}$$

$$\frac{s i_{g_q}}{\omega_b} = \frac{v_{v_q} - v_{e_q}}{L_{eq} + L_g} - \left(\frac{R_{eq} + R_g}{L_{eq} + L_g}\right) i_{g_q} - \omega_g i_{g_d} \tag{9}$$

where ω_b and ω_g represent the base frequency in rad/s and the grid-frequency in per-unit, respectively.

The active and reactive power formulas in SRF are given by:

$$P = v_{v_d} i_{g_d} + v_{v_q} i_{g_q} \tag{10}$$

The stored energy in upper/lower arms can be calculated as:

$$\dot{w_u} = \frac{1}{2} C_\sigma v_{c_u}^{\Sigma^2} = v_{z_j} i_{z_j}^\Sigma - \frac{1}{2} v_{v_j} i_{g_j} - v_{v_j} i_{z_j}^\Sigma + \frac{1}{2} v_{z_j} i_{g_j} \tag{11}$$

$$\dot{w_l} = \frac{1}{2} C_\sigma v_{c_l}^{\Sigma^2} = v_{z_j} i_{z_j}^\Sigma - \frac{1}{2} v_{v_j} i_{g_j} + v_{v_j} i_{z_j}^\Sigma - \frac{1}{2} v_{z_j} i_{g_j} \tag{12}$$

Referring to [23] , it can be convenient for control purposes to adopt a $(\Sigma - \Delta)$ representation for the energy as in (3)-(4), which yields:

$$\dot{w_j^\Sigma} = 2 v_{z_j}^\Sigma i_{z_j}^\Sigma - v_{v_j} i_{g_j} \tag{13}$$

$$\dot{w_j^\Delta} = -2 v_{v_j} i_{z_j}^\Sigma + v_{z_j}^\Sigma i_{g_j} \tag{14}$$

w_j^Σ and w_j^Δ represent the energy sum and difference between upper and lower arms, respectively.

Based on (3)-(14), the system state variables are the circulating currents i_z^Σ flowing through the filter L_{arm}, the grid current i_g flowing through the total equivalent impedance L_{eq}, L_g and the equivalent voltages v_c^Σ across the equivalent capacitors C_σ.

B. Grid-forming MMC Control

In this subsection, only the grid-forming capability is presented. The energy-based control of the MMC used in this paper is recalled on the appendix. Details on the used energy-based control structure can be found [25].

1) Active Power Control: In this paper, the outer active power controller is based on the PLL-free PI-controller [21]:

$$\omega_m = \left(\frac{P^* - P}{2Hs}\right) - k_p \cdot P \tag{15}$$

$$\theta_m = \omega_m \omega_b / s \tag{16}$$

with H, k_p and P^* denote the inertia constant, the damping factor and the active power setpoint, respectively. θ_m denotes the time-domain angle. In addition to the ability of the PI-controller to provide an inertial response, it takes the advantage of guaranteeing a decoupling between the active power regulation and the frequency support function exactly as a VSM [21], but without a need for a dedicated PLL, which makes the power control much simpler.

2) Voltage Generation: The AC voltage formed by the MMC is aligned on the $d - axis$ and directly driven to the modulation stage through the variable virtual impedance, which will be presented in the following subsection.

$$v_{v_d}^{**} = V_v^{**}, \;\; v_{v_q}^{**} = 0 \tag{17}$$

V^{**} denotes the AC voltage magnitude setpoint.

3) Variable Virtual impedance for current limitation (VI): To ease the understanding on the VI design, the MMC referring to [18] can be simply modeled as illustrated in Fig. 3, assuming that the internal energy of the MMC is well regulated and decoupled from the AC side. This assumption has been justified in [18] and will be also checked again in this paper through time-domain simulations. Let us consider the three

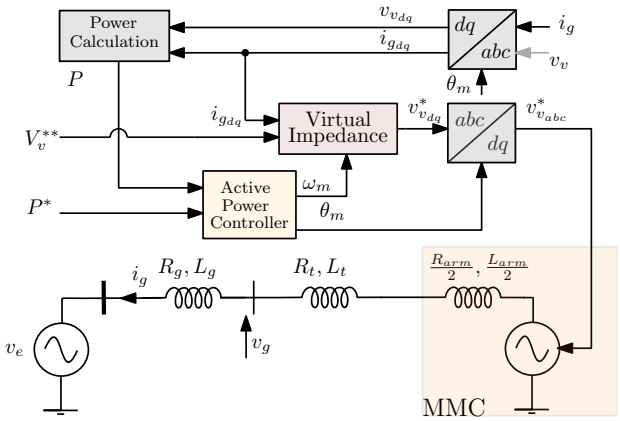

Fig. 3. Simplified representation of the grid-forming MMC

phase to ground fault at PCC level ($v_g = 0$ p.u) as depicted in Fig. 4. The idea behind the VI is to increase the output impedance of the system virtually when the fault is detected:

$$V_v^{**} = \sqrt{(X_{eq} + X_{VI})^2 + (X_{eq} + X_{VI})^2} I_g \tag{18}$$

Considering σ as X/R ratio, (18) can be written:

$$\left(\frac{V_v^{**}}{I_g}\right)^2 = (X_{eq} + X_{VI})^2 + (R_{eq} + X_{VI}\sigma^{-1})^2 \tag{19}$$

For $I_g = I_{max}$, the maximum virtual inductance $X_{VI_{max}}$ and $R_{VI_{max}}$ are obtained by solving equation (19):

$$X_{VI_{max}} = \frac{-B_{VI} - \Delta_{VI}}{2A_{VI}} \tag{20}$$

$$R_{VI_{max}} = X_{VI_{max}}\sigma^{-1} \tag{21}$$

where:

$$A_{VI} = 1 + \left(\sigma^{-1}\right)^2, \quad B_{VI} = 2X_{eq} + 2R_{eq}\sigma^{-1}$$

$$C_{VI} = X_{eq}^2 + R_{eq}^2 - \left(\frac{V_v^{**}}{I_{max}}\right)^2, \quad \Delta_{VI} = B_{VI}^2 - 4A_{VI}C_{VI}$$

Since the VI should only act on the system when the current exceeds its rated value ($I_n = 1$ p.u):

$$\{X_{VI}, R_{VI}\} = \begin{cases} \{X_{VI_{max}}, R_{VI_{max}}\} & \textbf{IF} \quad I_g = I_{max} \\ 0 & \textbf{IF} \quad I_g \leq I_n \end{cases} \tag{22}$$

To allow a smooth variation of the VI in the interval $[I_n, I_{max}]$, the adaptive coefficient k_R is defined as the ratio

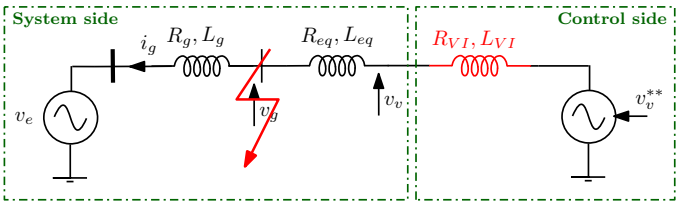

Fig. 4. Three-phase short circuit at PCC

that adapts the virtual impedance with respect to the current magnitude I_g and is given by:

$$k_R = \frac{R_{VI_{max}}}{I_{max} - I_n} = \frac{X_{VI_{max}}\sigma}{I_{max} - I_n} \tag{23}$$

From (20)-(23), the variable virtual impedance formula is obtained:

$$R_{VI} = \begin{cases} k_R(I_g - I_n) & \textbf{IF} \quad I_g > I_n \\ 0 & \textbf{IF} \quad I_g \leq I_n \end{cases} \tag{24}$$

$$X_{VI} = R_{VI}\sigma \tag{25}$$

Based on (24)-(25), the ratio σ is the only adjustable degree of freedom. In the next section, its impact on the system dynamics and the transient stability is investigated.

III. The Impact of the VI on the Small-Signal and Large-Signal Stability

A. Small-signal modeling and analysis

Note that the small-signal of a variable can be written as $x = x_0 + \Delta x$, where the index "0" and "Δ" denote the initial condition and the small variation around the operation point, respectively. To build the small-signal state space model of the MMC including the VI, the equations (8)-(10), (15)-(16) and (24)-(25) are linearized around $i_{g_{d_0}}, i_{g_{q_0}}$ as follows.
The active power equation in (8), (15)-(16) can be written:

$$\Delta P = \Delta v_{v_d} i_{g_{d0}} + \Delta i_{g_d} v_{v_{d0}} + \Delta v_{v_q} i_{g_{q0}} + \Delta i_{g_q} v_{v_{q0}} \tag{26}$$

$$\Delta\dot{\omega}_m = \frac{1}{2H}\left(\Delta P^* - \Delta P\right) \tag{27}$$

$$\Delta\dot{\delta}_m = -k_p \Delta P \omega_b + \Delta\omega_m \omega_b \tag{28}$$

with $\Delta\delta_m = \Delta\theta_m - \Delta\theta_g$.
The grid currents in (8-9) can be written:

$$\frac{\Delta\dot{i}_{g_d}}{\omega_b} = \frac{\Delta v_{v_d} - \Delta v_{e_d}}{L_{eq} + L_g} - \left(\frac{R_{eq} + R_g}{L_{eq} + L_g}\right)\Delta i_{g_d} + \omega_g \Delta i_{g_q} \tag{29}$$

$$\frac{\Delta\dot{i}_{g_q}}{\omega_b} = \frac{\Delta v_{v_q} - \Delta v_{e_q}}{L_{eq} + L_g} - \left(\frac{R_{eq} + R_g}{L_{eq} + L_g}\right)\Delta i_{g_q} - \omega_g \Delta i_{g_d} \tag{30}$$

with:

$$\Delta v_{e_d} = \Delta V_e \cos\left(\delta_{m_0}\right) - V_{e_0} \sin\left(\delta_{m_0}\right)\Delta\delta_m \tag{31}$$

$$\Delta v_{e_q} = \Delta V_e \sin\left(\delta_{m_0}\right) + V_{e_0} \cos\left(\delta_{m_0}\right)\Delta\delta_m \tag{32}$$

$$\Delta v_{v_d}^* = \Delta v_{v_d}^{**} - \Delta\delta v_{v_d} \tag{33}$$

$$\Delta v_{v_q}^* = -\Delta\delta v_{v_q} \tag{34}$$

$$\Delta\delta v_{v_d} = \Delta R_{VI} i_{g_{d0}} + \Delta i_{g_d} R_{VI_0} - \Delta X_{VI} i_{g_{q0}} + \Delta i_{g_q} X_{VI_0} \tag{35}$$

$$\Delta\delta v_{v_q} = \Delta R_{VI} i_{g_{q0}} + \Delta i_{g_q} R_{VI_0} + \Delta X_{VI} i_{g_{d0}} + \Delta i_{g_d} X_{VI_0} \tag{36}$$

In (35)-(36), R_{VI} and X_{VI} are considered as variables since they depend on the current magnitude I_g. From (24)-(25), the small-signal expressions of R_{VI} and X_{VI} are given by:

$$\Delta R_{VI} = k_R\left(\Delta I_g - \Delta I_n\right) \tag{37}$$

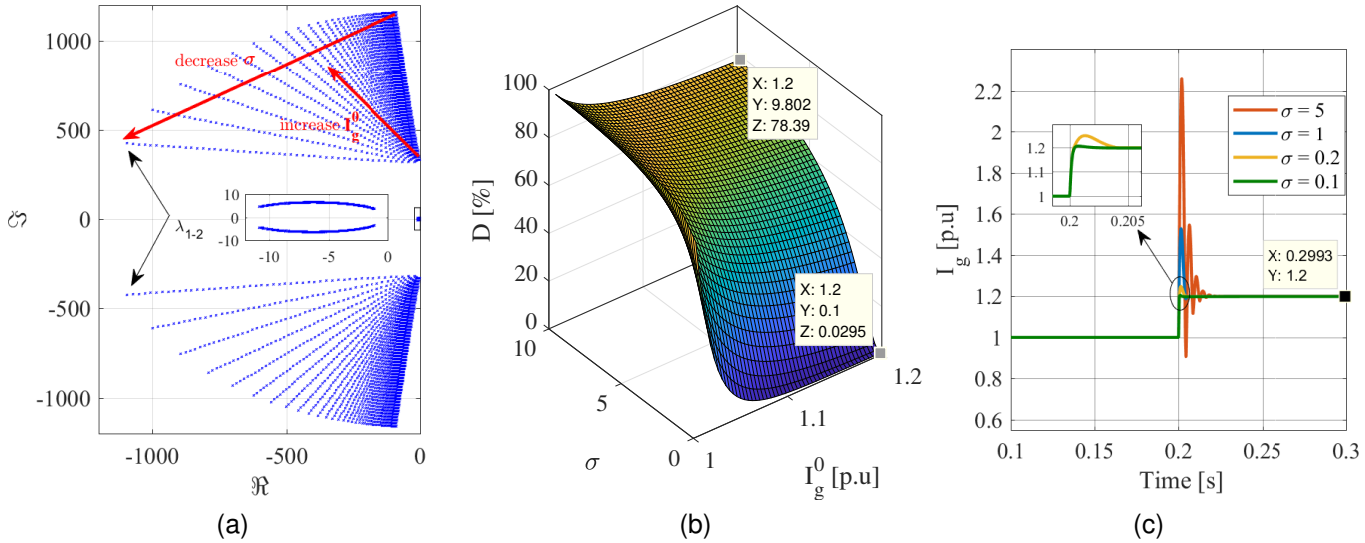

Fig. 5. System performances with respect to the operating point and the X/R ratio of the VI. (a) System modes. (b) Current Overshoot. (c) system response to a 100% voltage sag

$$A = \begin{bmatrix} -\frac{R_T\omega_b + R\omega_b}{L_T} & \omega_b\omega_0 - \frac{S\omega_b}{L_T} & \omega_b i_{g_{q0}} & \frac{\omega_b V_{e_0}\sin(\delta_{m0})}{L_T} \\ -\omega_b\omega_0 - \frac{V\omega_b}{L_T} & -\frac{R_T\omega_b + Q\omega_b}{L_T} & -\omega_b i_{g_{d0}} & \frac{\omega_b V_{e_0}\cos(\delta_{m0})}{L_T} \\ -\frac{v_{v_{d0}} + Ri_{g_{d0}} + VSi_{g_{q0}}}{2H} & -\frac{v_{v_{q0}} + Si_{g_{d0}} + Qi_{g_{q0}}}{2H} & 0 & 0 \\ -k_p\omega_b(v_{v_{d0}} + Ri_{g_{d0}} + VSi_{g_{q0}}) & -k_p\omega_b(v_{v_{q0}} + Si_{g_{d0}} + Qi_{g_{q0}}) & \omega_b & 0 \end{bmatrix}$$

$$B = \begin{bmatrix} \frac{\omega_b}{L_T} & -\frac{\omega_b\cos(\delta_{m0})}{L_T} & 0 \\ 0 & \frac{\omega_b\sin(\delta_{m0})}{L_T} & 0 \\ -\frac{i_{g_{d0}}}{2H} & 0 & \frac{1}{2H} \\ k_p\omega_b i_{g_{d0}} & 0 & 0 \end{bmatrix}, C = \begin{bmatrix} 1 & 0 & 0 & 0 \\ 0 & 1 & 0 & 0 \\ 0 & 0 & 1 & 0 \\ 0 & 0 & 0 & 1 \end{bmatrix}, D = \begin{bmatrix} 0 & 0 & 0 \\ 0 & 0 & 0 \\ 0 & 0 & 0 \\ 0 & 0 & 0 \end{bmatrix}$$

$$\Delta X_{VI} = k_R\left(\Delta I_g - \Delta I_n\right)\sigma \tag{38}$$

where:

$$\Delta I_g = \frac{i_{g_{d0}}}{I_{g_0}}\Delta i_{g_d} + \frac{i_{g_{q0}}}{I_{g_0}}\Delta i_{g_q} \tag{39}$$

By putting (39) in (37)-(38) and replace ΔR_{VI} and ΔX_{VI} in (33)-(34) by there expressions in (37)-(38), the generated voltage Δv_v^* in the SRF can written as:

$$\Delta v_{v_d}^* = \Delta v_{v_d}^{**} - R\Delta i_{g_d} - S\Delta i_{g_q} \tag{40}$$

$$\Delta v_{v_q}^* = -V\Delta i_{g_d} - Q\Delta i_{g_q} \tag{41}$$

with:

$$R = R_{VI_0} + k_R i_{g_{d0}}\left(\frac{i_{g_{d0}}}{I_{g_0}} - \frac{i_{g_{q0}}\sigma}{I_{g_0}}\right) - k_R i_{g_{d0}} \tag{42}$$

$$S = -X_{VI_0} + k_R i_{g_{q0}}\left(\frac{i_{g_{d0}}}{I_{g_0}} - \frac{i_{g_{q0}}\sigma}{I_{g_0}}\right) + k_R i_{g_{q0}}\sigma \tag{43}$$

$$V = X_{VI_0} + k_R i_{g_{d0}}\left(\frac{i_{g_{q0}}}{I_{g_0}} + \frac{i_{g_{d0}}\sigma}{I_{g_0}}\right) - k_R i_{g_{d0}}\sigma \tag{44}$$

$$Q = R_{VI_0} + k_R i_{g_{q0}}\left(\frac{i_{g_{q0}}}{I_{g_0}} + \frac{i_{g_{d0}}\sigma}{I_{g_0}}\right) - k_R i_{g_{q0}} \tag{45}$$

Considering the equations (26)-(45), the linear state-space representation of system and control equations are given by:

$$\begin{cases} \Delta\dot{\mathbf{x}} = \mathbf{A}\Delta\mathbf{x} + \mathbf{B}\Delta\mathbf{u} \\ \Delta\mathbf{y} = \mathbf{C}\Delta\mathbf{x} + \mathbf{D}\Delta\mathbf{u} \end{cases} \tag{46}$$

$$\Delta x = \begin{bmatrix}\Delta i_{g_d} & \Delta i_{g_q} & \Delta\omega_m & \Delta\delta_m\end{bmatrix}^T$$

$$\Delta u = \begin{bmatrix}\Delta V_v^{**} & \Delta V_e & \Delta P^*\end{bmatrix}^T$$

The control matrices A,B,C,D are given in the top of the page. One can notice from the control matrix A, that the system including the VI is highly dependant on the operation points. Moreover, it is simple to check the correctness of the developed calculation since, S and V, R and Q present respectively the virtual inductance and resistance, i.e., when $I_g = I_{max}$, $V = -S = X_{VI_{max}}$ and $R = Q = R_{VI_{max}}$.
Note also that the proposed state-space model is effective only when $I_{g_0} \geq I_n$, but, it could be used to analyse the system dynamics and stability in normal conditions by setting $k_R = 0$. Let us consider the system and control parameters listed in Table I. In Fig. 5a, a sensitivity analysis of $(I_{g0}, \sigma_{X/R})$ on the system eigenvalues evolution is performed. The obtained

TABLE I
SYSTEM AND CONTROL PARAMETERS

P_n	1000 MW	f_n	50 Hz
$\cos\phi$	0.95	U_e	320 kV
SCR	20	V_v^{**}	1 p.u
C_σ	0.12 mF	I_n	1 p.u
R_t	0.005 p.u	k_p	0.0159 p.u
L_t	0.15 p.u	L_{arm}	0.15 p.u
R_{arm}	0.005 p.u	H	5s
$T^R_{i^\Sigma_z}$	10 ms	I_{max}	1.2 p.u
u_{dc}	640 kV	$T^R_{w^\Delta}$	70m s
$T^R_{w^\Sigma}$	70 ms	ω^{Σ^*}	1 p.u
ω^{Δ^*}	0 p.u		

results show that for the operating conditions $I_{g0} = [I_n, I_{max}]$ and the ratio $\sigma = [0.1, 10]$, the system remains stable. On the other hand, the increase of the current magnitude in the defined range yields a damped λ_{1-2} corresponding to the state variables i_{gdq}. This result is more enhanced when the σ is decreasing. This statement can be either confirmed from the 3-D surface in Fig.5.b, where the overshoot defined from (47) is assessed with respect to the variation of σ and I_{g0} e.g., for $I_{g0} = I_{max}$ and $\sigma = 10$ the current overshoot is about 80%, whereas, for $I_{g0} = I_{max}$ and $\sigma = 0.1$ the current overshoot is about 0.03%.
The obtained theoretical results are supported by time domain-simulation in Fig.5c.

$$D_{[k]} = k \exp \frac{-\pi\zeta_{\lambda_{1-2}}}{\sqrt{1-\zeta^2_{\lambda_{1-2}}}} \quad \zeta_{\lambda_{1-2}} = \frac{-\Re}{\sqrt{\Re^2+\Im^2}} \tag{47}$$

ζ represents the damping coefficient. k factor equal 100.

B. Large-signal analysis

When subjected to a large disturbance the power inverter has to re-synchronize with the AC grid voltage using local measurements. The aim of this section is assess the transient stability of the system including the VI.
When the VI is deactivated, the quasi-static expression of the active power deduced from Fig. 3 is given by:

$$P = \underbrace{\frac{V_v V_g}{X_{eq}}}_{P_{max_1}} sin(\delta_m) \tag{48}$$

Based on (48), Fig. 6 depicts the (P-δ) curve of the grid-forming inverter. For a given P^*, there are two equilibrium points (a) and (a'), where the power P is equal to its reference P^*. However, only the equilibrium point (a) is stable from small-signal perspectives [7]. From large-signal perspective, the angle δ_{max} corresponding the equilibrium point a' is defined as the maximum angle guaranteeing the angle stability [7], [13] after a large disturbance, and it is given by:

$$\delta_{m_{max}} = \pi - \underbrace{\arcsin\left(\frac{P^*}{P_{max}}\right)}_{\delta_{m_0}} \tag{49}$$

With the introduction of the VI, the new quasi-static expression of the active power deduced from Fig. 4 is expressed as follow:

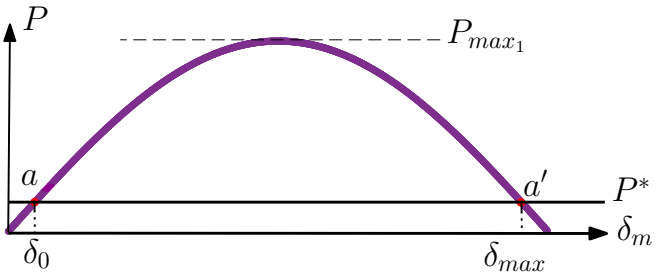

Fig. 6. $(P-\delta)$ curve

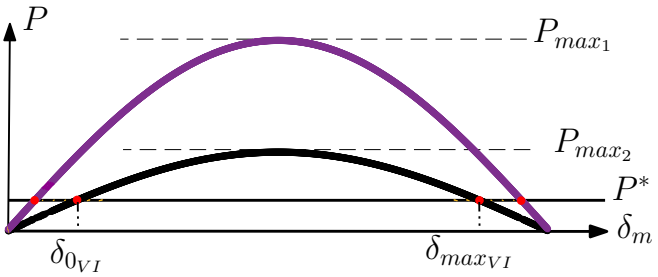

Fig. 7. $(P-\delta)$ curve including the VI

$$P = \frac{V^{**}V_g}{\sqrt{X_T^2+R_T^2}} \sin\left(\delta_m + \arctan\left(\frac{R_T}{X_T}\right)\right) - \frac{V_g^2 R_T}{X_T^2+R_T^2} \tag{50}$$

with $X_T = X_{eq} + X_{VI_{max}}$, $R_T = R_{eq} + R_{VI_{max}}$ where:

$$P_{max_2} = \frac{V^{**}V_g}{\sqrt{X_T^2+R_T^2}} - \frac{V_g^2 R_T}{X_T^2+R_T^2} \tag{51}$$

In the power transmission systems, the resistive effect is often neglected because of the high X/R ratio of the lines. In (50), the resistive effect is not neglected anymore because of the virtual impedance X_{VI}/R_{VI} that may be very small to enhance the grid current dynamics, as demonstrated in the previous subsection.
The activation of the VI results in a decrease of P_{max} to P_{max_2} since the total impedance increases. As a consequence, the maximum angle allowing a stable re-synchronization $\delta_{max_{VI}}$ will be decreased as illustrated in Fig. 7. It is given in this case by:

$$\delta_{max_{VI}} = 2\left(\frac{\pi}{2} - \arctan\left(\frac{R_T}{X_T}\right)\right) - \delta_{m_{0_{VI}}} \tag{52}$$

where:

$$\delta_{m_{0_{VI}}} = \arcsin\left[\left(P^* + \frac{V_e^2 R_T}{R_T^2+X_T^2}\right)\frac{\sqrt{X_T^2+R_T^2}}{V_v^{**}V_e}\right] - \arctan\left(\frac{R_T}{X_T}\right) \tag{53}$$

In Fig. 8, the $P-\delta$ curve including the VI has been drawn with respect to different values of $\sigma = [0.1, 10]$. One can notice that the decrease of σ yields a decrease of the maximum

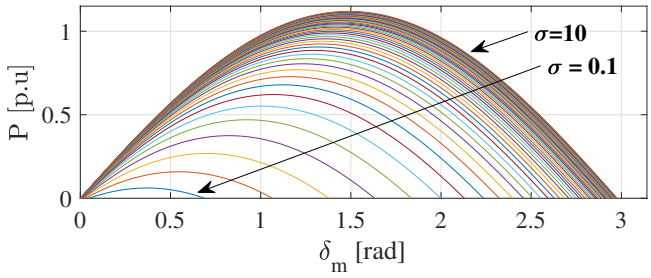

Fig. 8. $(P-\delta)$ curve including VI for various σ

transmissible active power and reduces the the maximum angle $\delta_{max_{VI}}$ e.g., if the operating point is initially set to P = 0.9 p.u, it can be deduced from (53) that the system has a chance reach-back its equilibrium point after a large disturbance, only and only if $\sigma \geq 2.7$, otherwise, the system leads automatically to instability.

Considering $\sigma \geq 2.7$, the conditions where the system do not exceed $\delta_{max_{VI}}$ depends on the fault type and its duration. These theoretical aspects will be extended and validated in the following section considering a practical case study.

1) case study - 100% grid voltage sag: Initially the inverter is operating in normal condition around its equilibrium point x_e (P_0 = 0.9 p.u corresponding to δ_{m_0} = 0.2453 rad/s), then, a voltage sag of 100% is applied:
From (50), the voltage drop ($v_g = 0$ p.u) results in a cancellation of the active power, which thereby yields a mismatch between the active power reference and the measured active power. According to the power control function in (15), the power mismatch results in a frequency deviation and consequently to the increase of the angle δ_m. Once the fault is cleared, the power angle remains increasing since $\Delta\omega_m$ stays greater than zero for a given duration because of the inertial effect. If the angle increase exceeds $\delta_{max_{VI}}$, the system leads to instability, otherwise, the angle starts to decrease when $\Delta\omega_m < 0$ until it reaches the equilibrium point x_e, where $P = P^*$ and $\Delta\omega_m = 0$ p.u. More details on the synchronization process of the grid-forming VSC can be found in [20].
The simulations in Fig. 9 comply with the described re-synchronization process, where the evolution of δ_m with respect to $\Delta\omega_m$ is drawn during the fault and the post-fault phases. Two fault durations were simulated, from which the effectiveness of the theoretical $\delta_{max_{VI}}$ that ensures the system stability has been proven (see the red and black curves). Note that it is also possible to notice that for $\sigma = 10$, the system remains stable for a fault duration of 141 ms. Whereas, with $\sigma = 3$, the system can only deal with 52ms. If σ is further decreased, the stability margin will be more restricted.

2) discussion: From Fig. 5 and Fig. 8, it is clear that σ has a contradictory effect on the grid current dynamics and the large-signal stability i.e., a small value of σ results in acceptable current dynamics and very limited transient stability margin and vice-versa.
It is possible to conclude at this stage that the conventional VI cannot cope at once with the current dynamics and the

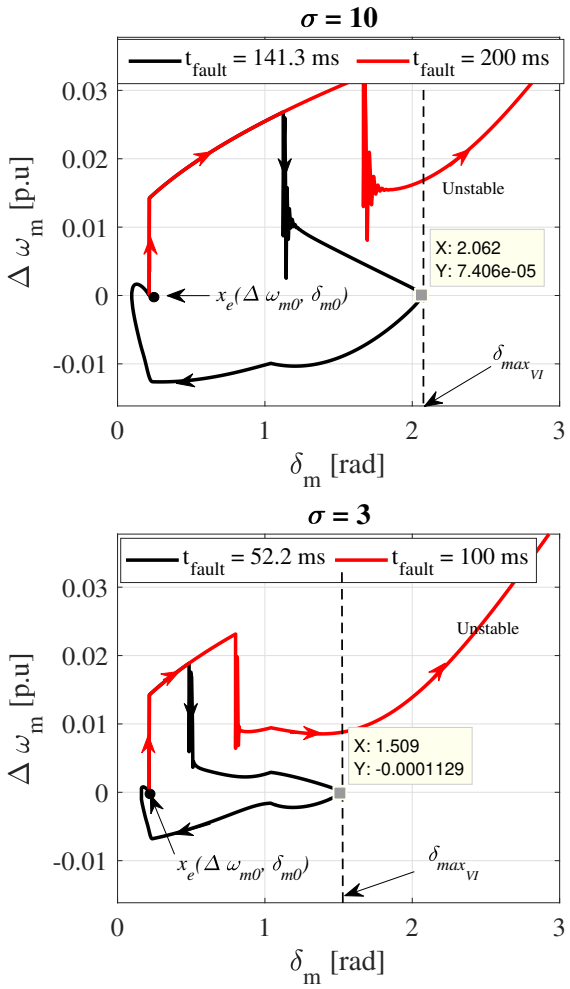

Fig. 9. $(\Delta\omega_m - \Delta\dot{\omega}_m)$ plan to evaluate the angular stability

transient stability without additional degrees of freedom. In the following section, an improved VI is proposed to enhance the grid current dynamics while guaranteeing the maximum transient stability margin allowed by the VI.

IV. Improved Variable Virtual Impedance

A. Variable Transient Virtual Resistance Design

From the prior analysis, it has been proven that higher $\sigma > 5$ yields an acceptable transient stability margin, but an oscillatory current behavior, while smaller σ yields a very limited transient stability margin, but well-damped currents. In this section, the idea behind the Variable Transient Virtual Resistance (VTVR) is to set a very low X/R in the transient in such a way as to damp the grid current, and a higher X/R in quasi-static and steady state in order to ensure the maximum stability margin allowed by the VI. The VTVR is given by the following formula:

$$R_{VTVR} = \begin{cases} \left(\dfrac{Ds}{s+\omega_D}\right)(I_g - I_n) & \textbf{IF} \quad I_g > I_n \\ 0 & \textbf{IF} \quad I_g \leq I_n \end{cases} \tag{54}$$

D and ω_D denote the damping factor and the cut-off frequency of the high-pass filter (HPF), respectively.

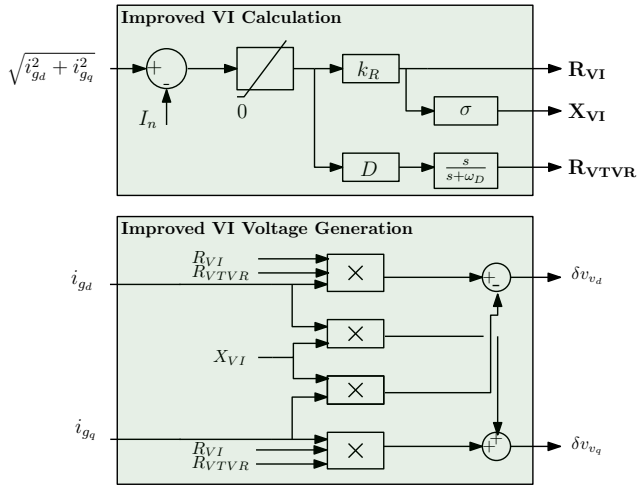

Fig. 10. Improved Variable Virtual Impedance

To design, R_{VTVR}, a new variable defined as the transient X/R ratio is introduced:

$$\sigma_{TR} = \frac{X_{VI}}{R_{VI} + R_{VTVR}} \tag{55}$$

In steady-state, $\sigma_{TR} = \sigma$ since R_{VTVR} will be cancelled because of the HPF.

Based on the desired dynamic performances, the parameters of the improved variable virtual impedance can be determined, i.e., the R_{VI}, X_{VI} can be determined from (24)-(25) and D can be determined from the following equations:

$$\sigma_{TR} = \frac{\sigma}{1 + \frac{D}{R_{VI_{max}}}} \tag{56}$$

which yields,

$$D = R_{VI_{max}} \left(\frac{\sigma}{\sigma_{TR}} - 1 \right) \tag{57}$$

The cut-off frequency of the HPF can be chosen simply so as D has an effect on the current dynamics only during the first fault instants (e.g., $\omega_D = 1e^3$ rad/s).

The illustration of the improved VI is shown in Fig. 10.

B. Practical case study and comparison

In this subsection, the aim is to validate the proposed theoretical approaches considering all the MMC dynamics and show the effectiveness of the proposed VI. The grid case in Fig. 11 is used. The test case performed in this subsection

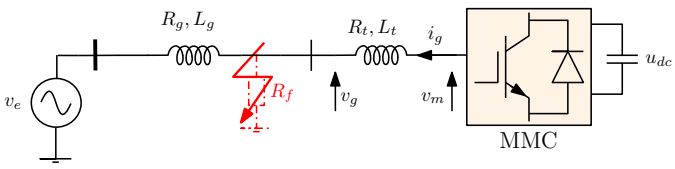

Fig. 11. Fault Evaluation at PCC

assesses the system behavior under a three-phase impedant fault ($R_f = 0$) at PCC while comparing the proposed method

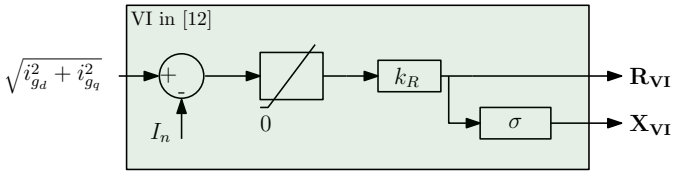

Fig. 12. Variable Virtual Impedance proposed in [12]

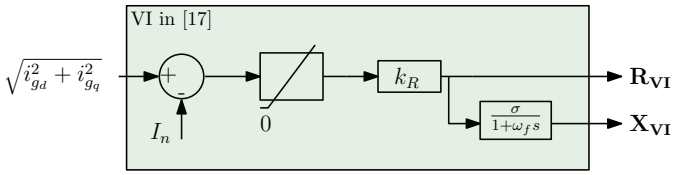

Fig. 13. Variable Virtual Impedance proposed in [17]

to the ones in [12] and [17]. The latter are recalled in Fig. 12 and Fig. 13, respectively.

The operating point is initially set to $P_0 = 0.6$ p.u, then a 140ms fault is applied at t = 1.2s. The results are gathered in Fig. 14 and Fig. 15, respectively. The following quantities are simulated: the grid current i_g, the output voltage v_m and the equivalent capacitor voltages $v_{c_{u/l}}^{\Sigma}$.

The results in Fig.14.A show that the method proposed in [12] presents an oscillatory behavior for $\sigma = 8$, which is reflected on the output current and voltage. The current based on this method reaches 1.67 p.u in the transient before reaching its reference $I_{max} = 1.2$ p.u within 50ms. During the post-fault phase, the system recovers stably its equilibrium point. In Fig.15.A, the ratio σ has been reduced to $\sigma = 0.1$, which widely improves the current dynamics, however, the system looses the synchronism and leads to transient instability. Despite that the dynamic performances with the VI in [17] shown in Fig.14.B are much higher than the ones in Fig.14.A thanks to the additional low-pass filter on the X_{VI} (with $\omega_f = 2\pi 10$ rad/s [17]), the transient current peak is still higher than the maximum allowable current (i.e., 1.92 p.u for $\sigma = 8$), which affect the inverter reliability. The current peak can be reduced by reducing σ, however, this yields a transient instability as shown in Fig.15.A, Fig.15.B and which has been demonstrated along this paper.

The results in Fig.14.C and Fig.15.C show the advantage the proposed VI takes over the conventional VI methods. Thanks to the additional degree of freedom σ_{TR}, the current dynamics can be improved without affecting transient stability.

V. Conclusion

In this paper, small and large-signal models of the grid-forming modular multilevel inverter embedding the variable virtual impedance for current limitation have been developed and discussed. It has been shown that the ratio X/R of the virtual impedance has a contradictory effect on the grid current dynamics and the angle stability. This issue has been solved in this paper through an additional variable transient virtual resistance, which damps the current transients without affecting the transient stability allowed with higher X/R ratios. The performances and the effectiveness of the proposed method

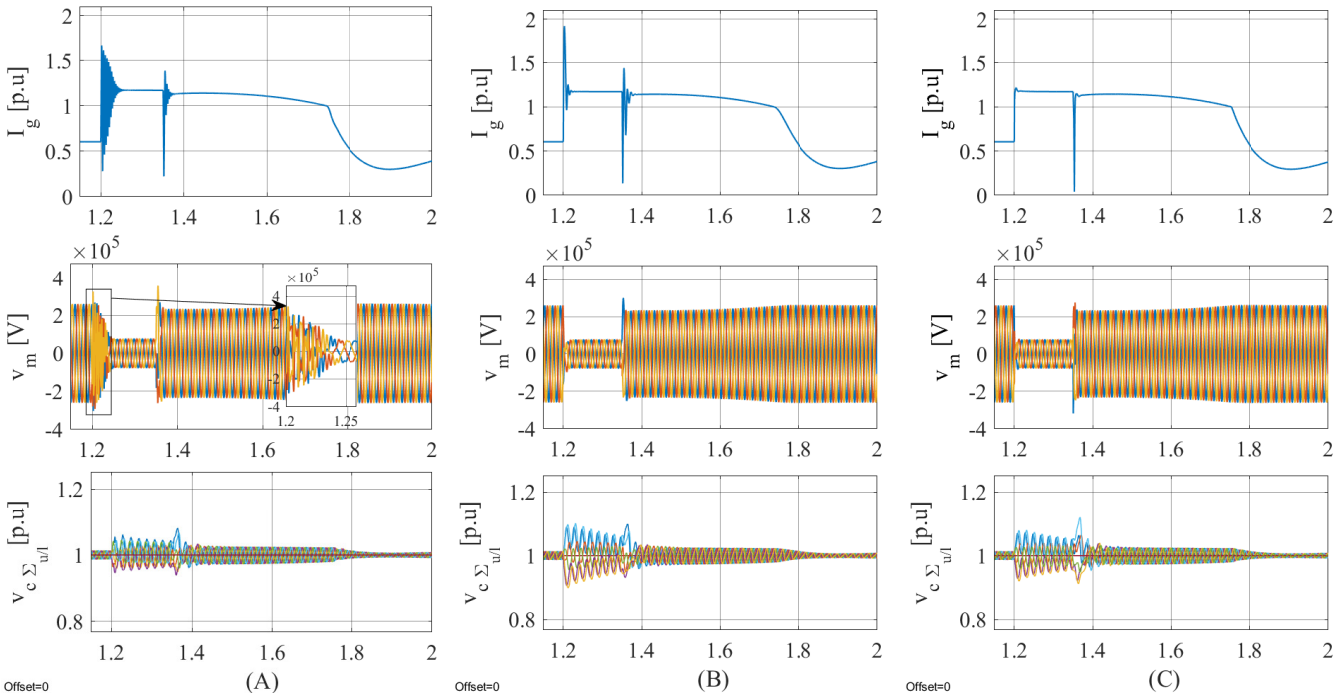

Fig. 14. 140ms three-phase fault, (A) The VI in [12] with $\sigma = 8$, (B), The VI in [17] with $\sigma = 8$, (C) The proposed VI with $\sigma = 8$ and $\sigma_{TR} = 0.1$

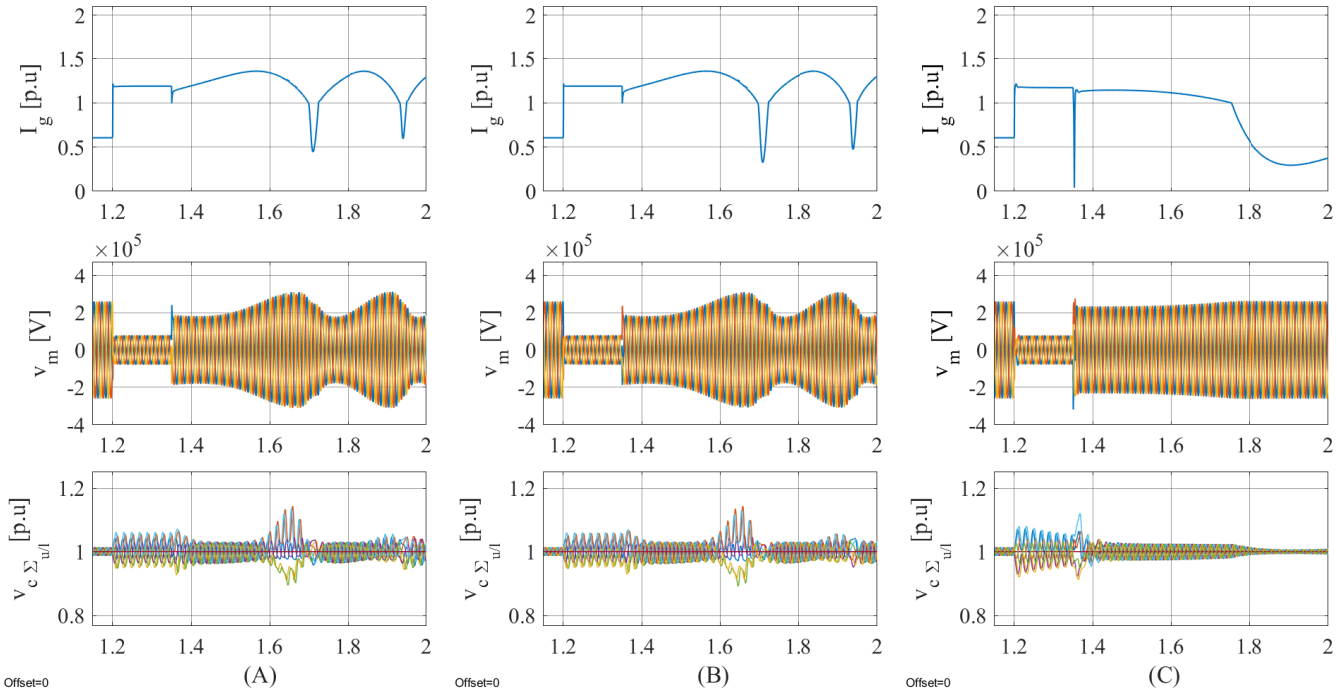

Fig. 15. 140ms three-phase fault, (A) The VI in [12] with $\sigma = 0.1$, (B), The VI in [17] with $\sigma = 0.1$, (C) The proposed VI with $\sigma = 8$ and $\sigma_{TR} = 0.1$

have been demonstrated theoretically and through time-domain simulations.

Future works can be devoted to combine the proposed VI with additional algorithms that avoid the frequency deviation in order to more improve the transient stability. Additionally, the proposed method can be extended to unbalanced grid conditions.

APPENDIX

The differential currents i_z^{Σ} are controlled via three parallel PI-controllers to determine the the voltage reference v_z^*:

$$v_{z_j}^* = \left(k_p^z + \frac{k_i^z}{s}\right)\left(i_{z_j}^{\Sigma *} - i_{z_j}^{\Sigma}\right) + \frac{v_{dc}}{2} \tag{58}$$

The circulating current's references consist of a DC components $i_{z_{DC}}^{\Sigma *} = i_{dc}/3$ and a circulating AC components $i_{z_{AC}}^{\Sigma *}$

rotating with -2ω:

$$i_{z_j}^{\Sigma*} = i_{z_{j\,DC}}^{\Sigma*} + i_{z_{j\,AC}}^{\Sigma*} \tag{59}$$

The AC and DC of the differential current components are generated by the horizontal and vertical energy-based control given by:

$$i_{z_{j\,DC}}^{\Sigma*} * = \left[\left(k_p^{\Sigma} + \frac{k_i^{\Sigma}}{s}\right)\left(\omega_j^{\Sigma*} - \bar{\omega_j^{\Sigma}}\right) + \frac{P}{3}\right] v_{dc} \tag{60}$$

$$i_{z_{j\,AC}}^{\Sigma*} = \left[\left(k_p^{\Delta} + \frac{k_i^{\Delta}}{s}\right)\left(\omega_j^{\Delta*} - \bar{\omega_j^{\Delta}}\right)\frac{\sqrt{2}}{V_g}\right]\kappa \tag{61}$$

with:

$$\kappa = \begin{bmatrix} \sin(\omega_m t) & 0 & 0 \\ 0 & \sin(\omega_m t - \frac{2\pi}{3}) & 0 \\ 0 & 0 & \sin(\omega_m t + \frac{2\pi}{3}) \end{bmatrix}$$

Note that $\bar{\omega_j^{\Sigma}}$ and $\bar{\omega_j^{\Delta}}$ are filtered using a moving average filters (MAF) of 100Hz and 50 Hz, respectively.

Based on $v_{v_j}^*$ generated by the grid-forming control and $v_{z_j}^*$ in (58), the upper and lower modulated voltage are determined:

$$v_{m_{u_j}}^* = v_{z_j}^* - v_{v_j}^* \tag{62}$$

$$v_{m_{l_j}}^* = v_{z_j}^* + v_{v_j}^* \tag{63}$$

REFERENCES

[1] T. QORIA, "Grid-forming control to achieve a 100% power electronics interfaced power transmission systems," ENSAM, Paris, 2020.

[2] S. D'Arco and J. A. Suul, "Equivalence of Virtual Synchronous Machines and Frequency-Droops for Converter-Based MicroGrids," IEEE Trans. Smart Grid, vol. 5, no. 1, pp. 394–395, Jan. 2014, doi: 10.1109/TSG.2013.2288000.

[3] J. Liu, Y. Miura, and T. Ise, "Comparison of Dynamic Characteristics Between Virtual Synchronous Generator and Droop Control in converter-Based Distributed Generators," IEEE Trans. Power Electron., vol. 31, no. 5, pp. 3600–3611, May 2016, doi: 10.1109/TPEL.2015.2465852.

[4] H. -P. Beck and R. Hesse, "Virtual synchronous machine," 2007 9th International Conference on Electrical Power Quality and Utilisation, 2007, pp. 1-6, doi: 10.1109/EPQU.2007.4424220.

[5] H2020 MIGRATE PROJECT https://www.h2020-migrate.eu/

[6] "AN2011-05 Industrial IGBT Modules Explanation of Technical Information", Infineon Technical report, November 2015,

[7] L. Huang, H. Xin, Z. Wang, L. Zhang, K. Wu, and J. Hu, "Transient Stability Analysis and Control Design of Droop-Controlled Voltage Source Converters Considering Current Limitation," in *IEEE Trans. Smart Grid*, vol. 10, no. 1, pp. 578–591, Sep. 2017.

[8] I. Sadeghkhani, M. E. Hamedani Golshan, J. M. Guerrero and A. Mehrizi-Sani, "A Current Limiting Strategy to Improve Fault Ride-Through of Inverter Interfaced Autonomous Microgrids," in IEEE Transactions on Smart Grid, vol. 8, no. 5, pp. 2138-2148, Sept. 2017, doi: 10.1109/TSG.2016.2517201.

[9] E. Rokrok, T. Qoria, A. Bruyere, B. Francois and X. Guillaud, "Transient Stability Assessment and Enhancement of Grid-Forming Converters Embedding Current Reference Saturation as Current Limiting Strategy," in IEEE Transactions on Power Systems, doi: 10.1109/TPWRS.2021.3107959

[10] M. G. Taul, X. Wang, P. Davari and F. Blaabjerg, "Current Limiting Control With Enhanced Dynamics of Grid-Forming Converters During Fault Conditions," in IEEE Journal of Emerging and Selected Topics in Power Electronics, vol. 8, no. 2, pp. 1062-1073, June 2020, doi: 10.1109/JESTPE.2019.2931477.

[11] J. Freytes, J. Li, G. de Préville and M. Thouvenin, "Grid-Forming Control With Current Limitation for MMC Under Unbalanced Fault Ride-Through," in IEEE Transactions on Power Delivery, vol. 36, no. 3, pp. 1914-1916, June 2021, doi: 10.1109/TPWRD.2021.3053148

[12] A. D. Paquette and D. M. Divan, "Virtual Impedance Current Limiting for Inverters in Microgrids With Synchronous Generators," *IEEE Trans. Ind. Appl.*, vol. 51, no. 2, pp. 1630–1638, Mar. 2015.

[13] Taoufik Qoria, François Gruson, Fréderic Colas, Xavier Kestelyn, Xavier Guillaud, "Current limiting algorithms and transient stability analysis of grid-forming VSCs", Electric Power Systems Research, Volume 189, 2020, 106726, ISSN 0378-7796,

[14] G. Denis, T. Prevost, M. S. Debry, F. Xavier, X. Guillaud, and A. Menze, "The migrate project: the challenges of operating a transmission grid with only inverter-based generation. a grid-forming control improvement with transient current-limiting control," IET Renewable Power Generation, vol. 12, no. 5, pp. 523–529, 2018.

[15] X. Wang, Y. W. Li, F. Blaabjerg and P. C. Loh, "Virtual-Impedance-Based Control for Voltage-Source and Current-Source Converters," in IEEE Transactions on Power Electronics, vol. 30, no. 12, pp. 7019-7037, Dec. 2015, doi: 10.1109/TPEL.2014.2382565.

[16] Qoria, T., Li, C., Oue, K. et al. Direct AC voltage control for grid-forming inverters. J. Power Electron. 20, 198–211 (2020). https://doi.org/10.1007/s43236-019-00015-4

[17] H. Wu and X. Wang, "Small-Signal Modeling and Controller Parameters Tuning of Grid-Forming VSCs with Adaptive Virtual Impedance-Based Current Limitation," in IEEE Transactions on Power Electronics, doi: 10.1109/TPEL.2021.3135693.

[18] E. Rokrok et al., "Impact of grid-forming control on the internal energy of a modular multilevel converter," 2020 22nd European Conference on Power Electronics and Applications (EPE'20 ECCE Europe), 2020, pp. 1-10,

[19] Z. Shuai, C. Shen, X. Liu, Z. Li, and Z. John Shen, "Transient angle stability of virtual synchronous generators using Lyapunov's direct method," *IEEE Trans. Smart Grid*, vol. 10, no. 4, pp. 4648–4661, 2019.

[20] T. Qoria, F. Gruson, F. Colas, G. Denis, T. Prevost, and X. Guillaud, "Critical clearing time determination and enhancement of grid-forming converters embedding virtual impedance as current limitation algorithm," *IEEE J. Emerg. Sel. Top. Power Electron.*, vol. 8, no. 2, pp. 1050–1061, Jun. 2020.

[21] T. Qoria, E. Rokrok, A. Bruyere, B. Francois, and X. Guillaud, "A PLL-Free Grid-Forming Control with Decoupled Functionalities for High-Power Transmission System Applications," *IEEE Access*, vol. 8, pp. 197363–197378, Oct. 2019.

[22] X. Wang, M. G. Taul, H. Wu, Y. Liao, F. Blaabjerg and L. Harnefors, "Grid-Synchronization Stability of Converter-Based Resources—An Overview," in IEEE Open Journal of Industry Applications, vol. 1, pp. 115-134, 2020, doi: 10.1109/OJIA.2020.302039

[23] G. Bergna-Diaz, J. Freytes, X. Guillaud, S. D. Arco and J. A. Suul, "Analysis of MMC Dynamics in DQZ Coordinates for Vertical and Horizontal Energy Balancing Control," IECON 2018 - 44th Annual Conference of the IEEE Industrial Electronics Society, 2018, pp. 5999-6006, doi: 10.1109/IECON.2018.8592881.

[24] D. Pan, X. Wang, F. Liu, and R. Shi, "Transient Stability Impact of Reactive Power Control on Grid-Connected Converters," in Proc. IEEE Energy Conversion Congress and Exposition (ECCE), Baltimore, MD, USA, 2019, pp. 4311–4316.

[25] S. Samimi, F. Gruson, P. Delarue, F. Colas, M. M. Belhaouane and X. Guillaud, "MMC Stored Energy Participation to the DC Bus Voltage Control in an HVDC Link," in IEEE Transactions on Power Delivery, vol. 31, no. 4, pp. 1710-1718, Aug. 2016, doi: 10.1109/TPWRD.2016.2540926.